

Optimizing the Acquisition Geometry for Digital Breast Tomosynthesis Using the Defrise Phantom

Raymond J. Acciavatti, Alice Chang, Laura Woodbridge, and Andrew D. A. Maidment
University of Pennsylvania, Department of Radiology, 3400 Spruce St., Philadelphia PA 19104
E-mail: Raymond.Acciavatti@uphs.upenn.edu, calic@seas.upenn.edu,
wolau@seas.upenn.edu, Andrew.Maidment@uphs.upenn.edu

ABSTRACT

In cone beam computed tomography (CT), it is common practice to use the Defrise phantom for image quality assessment. The phantom consists of a stack of plastic plates with low frequency spacing. Because the x-ray beam may traverse multiple plates, the spacing between plates can appear blurry in the reconstruction, and hence modulation provides a measure of image quality. This study considers the potential merit of using the Defrise phantom in digital breast tomosynthesis (DBT), a modality with a smaller projection range than CT. To this end, a Defrise phantom was constructed and subsequently imaged with a commercial DBT system. It was demonstrated that modulation is dependent on position and orientation in the reconstruction. Modulation is preserved over a broad range of positions along the chest wall if the input frequency is oriented in the tube travel direction. By contrast, modulation is degraded with increasing distance from the chest wall if the input frequency is oriented in the posteroanterior (PA) direction. A theoretical framework was then developed to model these results. Reconstructions were calculated in an acquisition geometry designed to improve modulation. Unlike current geometries in which the x-ray tube motion is restricted to the plane of the chest wall, we consider a geometry with an additional component of tube motion along the PA direction. In simulations, it is shown that the newly proposed geometry improves modulation at positions distal to the chest wall. In conclusion, this study demonstrates that the Defrise phantom is a tool for optimizing DBT systems.

Keywords: Defrise phantom, image quality, modulation, digital breast tomosynthesis (DBT), reconstruction, anisotropy, analytical modeling, optimization.

1. INTRODUCTION

It is common practice to use the Defrise phantom for assessing image quality in cone beam computed tomography (CT). One application of the Defrise phantom is comparing the benefits of various reconstruction algorithms in CT.¹ In this study, we consider the potential merit of using the Defrise phantom in digital breast tomosynthesis (DBT), which acquires projection images over a smaller angular range than CT.

We have experimentally analyzed a Defrise phantom using a commercial DBT system (Selenia Dimensions, Hologic Inc., Bedford, MA). The phantom was built using a laser cutter to create 10 plastic rectangular plates (15.0 cm \times 5.0 cm \times 0.29 cm) with a constant air gap (0.29 cm). The phantom was placed at various positions along the chest wall side of the DBT system, with the plastic-air spacings oriented along the tube travel direction. Images were acquired at 33 kVp and 59 mAs with a W/AI target-filter combination. With the phantom centered at the chest wall, Figure 1(a) shows a slice along the mid-depth of the object using the Selenia Dimensions reconstruction algorithm. The resultant signal profile [Figure 2(a)] can be used to quantify the image quality. In particular, the peak-to-peak amplitude (Pk-Pk) measures the relative ability to discern the plastic-air spacings. Figure 2(b) illustrates that image quality is preserved at various positions along the chest wall. The change in Pk-Pk varies between +38.6% and -5.8% relative to the midpoint of the chest wall.

To determine whether image quality is preserved in other directions, the Defrise phantom was rotated by 90°, so that the plastic-air spacings were oriented along the posteroanterior (PA) direction (*i.e.*, the direction perpendicular to the plane of x-ray tube motion). Because different filtering is applied in this direction in the reconstruction, Pk-Pk is plotted on a different scale. Comparing Figure 1(b) with Figure 2(b) shows that Pk-Pk is degraded with increasing PA position, indicating poor image quality. The edges of the phantom also show blurring artifacts along this direction [Figure 1(b)].

These results demonstrate that the Defrise phantom can be used to analyze the spatial anisotropy of image quality in DBT.

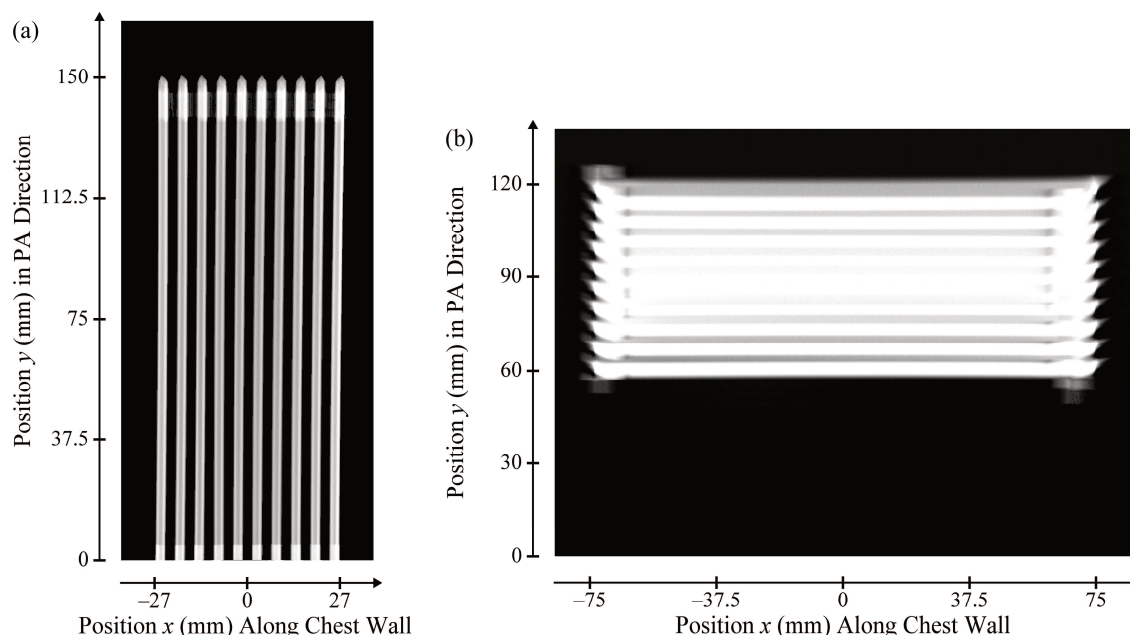


Figure 1. (a) A slice at the mid-depth of the reconstructed volume is shown for a Defrise phantom whose input frequency is oriented along the x direction (*i.e.*, tube travel direction). (b) By rotating the phantom by 90° , the image quality can be analyzed along the y direction (*i.e.*, PA direction). Unlike image (a), image (b) shows blurring artifacts, indicating poor image quality.

In DBT, projections are acquired as the x-ray tube traces a circular arc within the plane of the chest wall. The purpose of this study is to demonstrate that image quality can be improved by introducing an additional component of x-ray tube motion perpendicular to the chest wall. Accordingly, we model multiple acquisition geometries with tube motion along the PA direction. For various candidate geometries, the system design is evaluated by calculating modulation in the reconstruction of a thick sinusoidal test object oriented along the PA direction. This object provides a framework for simulating a Defrise phantom.

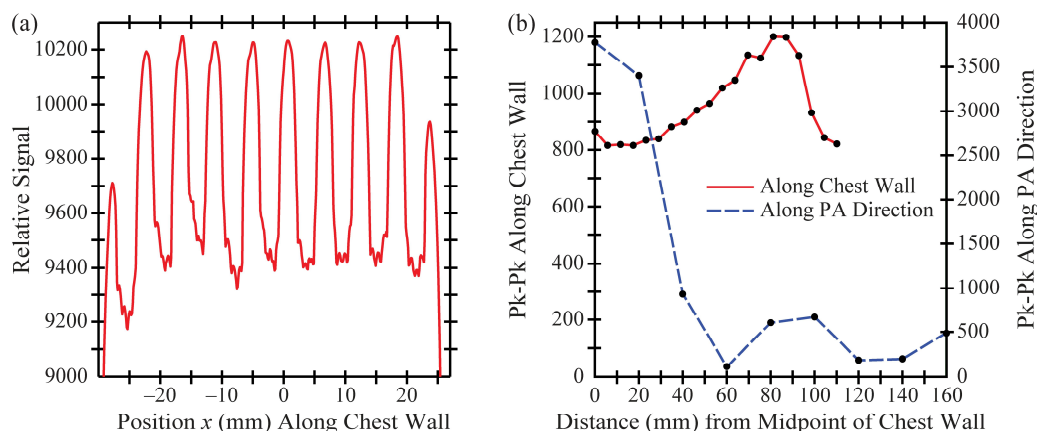


Figure 2. (a) The signal profile is calculated to quantify the image quality along the x direction as shown in Figure 1(a). (b) In the signal profile, the peak-to-peak amplitude (Pk-Pk) measures the ability to discern the plastic-air spacings in the Defrise phantom. The degradation in Pk-Pk along the PA direction indicates a loss of image quality at positions distal to the chest wall.

2. METHODS

2.1 Calculation of the Projection Images

An analytical model of the Defrise phantom is developed by calculating the reconstruction of a sinusoidal test object. Although the attenuation coefficient of the experimental phantom is step-like due to the discrete spacing between the plastic plates, it is useful to treat the attenuation coefficient as a smooth function in developing the analytical model. As such, the object is modeled as a rectangular prism whose attenuation coefficient varies sinusoidally along the y direction (*i.e.*, PA direction). Defining the xz plane as the chest wall (Figure 3), it is assumed that the object has extent along the source-to-support (SS) direction between the heights $z = z_0 \pm \varepsilon/2$ above the detector, where z_0 is the central height of the input object and ε is its thickness. The linear attenuation coefficient $\mu(x, y, z)$ of this object is thus

$$\mu(x, y, z) = C \cdot \cos[2\pi f_0(y - y_0)] \cdot \text{rect}\left(\frac{z - z_0}{\varepsilon}\right), \quad (1)$$

where C is the amplitude of the waveform, f_0 is the frequency, and y_0 is a translational shift in the position of the waveform. In current DBT systems, projection images are acquired as the x-ray tube rotates in a circular arc within the plane of the chest wall. A more general form of x-ray tube motion is now modeled, in which the vector from the origin O (*i.e.*, the midpoint of the chest wall side of the detector) to any point A in the x-ray tube trajectory is written as

$$\overline{OA} = x_{\text{FS}}(n)\mathbf{i} + y_{\text{FS}}(n)\mathbf{j} + z_{\text{FS}}(n)\mathbf{k}, \quad (2)$$

where ‘‘FS’’ denotes the most general focal spot position along the x , y , and z directions for the n^{th} projection. Assuming that the detector is stationary during the scan time, the vector from O to an arbitrary point on the detector (point B) can be defined as: $\overline{OB} = u_1\mathbf{i} + u_2\mathbf{j}$. Combining this expression with Eq. (2) yields the vector from point B on the detector to the focal spot at A .

$$\overline{BA} = -\overline{OB} + \overline{OA} = [x_{\text{FS}}(n) - u_1]\mathbf{i} + [y_{\text{FS}}(n) - u_2]\mathbf{j} + z_{\text{FS}}(n)\mathbf{k} \quad (3)$$

Using Eq. (3), the incident angle relative to the normal to the detector can be evaluated from the dot product

$$\cos\theta_n = \frac{\overline{BA} \cdot \mathbf{k}}{|\overline{BA}| |\mathbf{k}|}, \quad \theta_n = \arccos\left(\frac{z_{\text{FS}}(n)}{\sqrt{[x_{\text{FS}}(n) - u_1]^2 + [y_{\text{FS}}(n) - u_2]^2 + [z_{\text{FS}}(n)]^2}}\right). \quad (4)$$

The detector signal for each projection can now be determined by tracing the ray between points A and B . Defining w to be a free parameter, the equation of the ray can be written

$$\begin{pmatrix} x \\ y \\ z \end{pmatrix} = w \begin{pmatrix} u_1 - x_{\text{FS}}(n) \\ u_2 - y_{\text{FS}}(n) \\ -z_{\text{FS}}(n) \end{pmatrix} + \begin{pmatrix} x_{\text{FS}}(n) \\ y_{\text{FS}}(n) \\ z_{\text{FS}}(n) \end{pmatrix}, \quad w \in [0, 1]. \quad (5)$$

The focal spot at A has been defined to correspond with $w = 0$, and the incident point at B has been defined to correspond with $w = 1$. The x-ray path length \mathcal{L}_n through the object for the n^{th} projection is determined from the intersection of Eq. (5) with the planes $z = z_0 \pm \varepsilon/2$. The values of w for these two points are $w_n^{\pm} = 1 - (z_0 \pm \varepsilon/2)/z_{\text{FS}}(n)$. For the n^{th} projection, total attenuation $\mathcal{A}\mu(n)$ is found by integrating $\mu(x, y, z)$ along \mathcal{L}_n

$$\mathcal{A}\mu(n) = \int_{\mathcal{L}_n} \mu ds, \quad ds = \sqrt{\left(\frac{dx}{dw}\right)^2 + \left(\frac{dy}{dw}\right)^2 + \left(\frac{dz}{dw}\right)^2} dw = z_{\text{FS}}(n) \cdot \sec(\theta_n) dw, \quad (6)$$

where ds denotes the differential arc length along \mathcal{L}_n . Combining Eqs. (1), (5), and (6) yields the total x-ray attenuation at the detector point (u_1, u_2) for the n^{th} projection

$$\mathcal{A}\mu(n) = \kappa_n \int_{w_n^+}^{w_n^-} \cos(2\pi f_0 [u_2 - y_{\text{FS}}(n)]w + \lambda_n) dw \quad (7)$$

$$= \frac{\kappa_n \left(\sin(2\pi f_0 [u_2 - y_{\text{FS}}(n)]w_n^- + \lambda_n) - \sin(2\pi f_0 [u_2 - y_{\text{FS}}(n)]w_n^+ + \lambda_n) \right)}{2\pi f_0 [u_2 - y_{\text{FS}}(n)]}, \quad (8)$$

where

$$\kappa_n = C \cdot z_{\text{FS}}(n) \cdot \sec(\theta_n), \quad \lambda_n = 2\pi f_0 [y_{\text{FS}}(n) - y_0]. \quad (9)$$

To simplify Eq. (8), recall the identity: $\sin(b_1) - \sin(b_2) = 2\cos[(b_1 + b_2)/2]\sin[(b_1 - b_2)/2]$. Thus

$$\mathcal{A}\mu(n) = \kappa_n (w_n^- - w_n^+) \cdot \cos(\pi f_0 [u_2 - y_{\text{FS}}(n)] [w_n^+ + w_n^-] + \lambda_n) \cdot \text{sinc}(f_0 [u_2 - y_{\text{FS}}(n)] [w_n^- - w_n^+]) \quad (10)$$

$$= \frac{\varepsilon \kappa_n}{z_{\text{FS}}(n)} \cdot \cos\left(2\pi f_0 [u_2 - y_{\text{FS}}(n)] \left[1 - \frac{z_0}{z_{\text{FS}}(n)}\right] + \lambda_n\right) \cdot \text{sinc}\left(\frac{\varepsilon f_0}{z_{\text{FS}}(n)} [u_2 - y_{\text{FS}}(n)]\right), \quad (11)$$

where $\text{sinc}(u) \equiv \sin(\pi u)/(\pi u)$. This expression for total attenuation implicitly assumes that the x-ray converter has a modulation transfer function (MTF) of unity at all frequencies, and hence a point spread function (PSF) given by a delta function. Lee *et al.* demonstrated that an amorphous selenium (*a*-Se) photoconductor operated in drift mode is a good approximation for a detector material with these properties.² To take into account the presence of a thin-film transistor (TFT) array, the signal in the x-ray converter [Eq. (11)] must be sampled in detector elements. Following our previous work, detector elements are taken to be rectangular with sides of length $a_x \times a_y$, and are centered on the coordinates $u_1 = m_x a$ and $u_2 = (m_y + 1/2)a$, where m_x is an integer and m_y is a non-negative integer. The logarithmically-transformed signal is calculated by averaging signal over the \mathbf{m}^{th} detector element [Eq. (31) in Acciavatti and Maidment³].

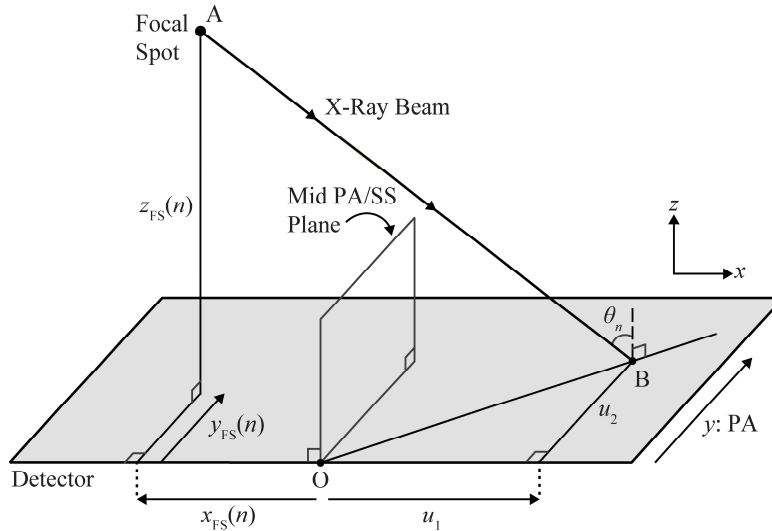


Figure 3. An acquisition geometry for DBT is modeled with the most general focal spot (FS) positions, assuming a stationary detector. This geometry differs from existing DBT systems, in which the focal spot motion is restricted to the plane of the chest wall (*i.e.*, the xz plane).

2.2 Filtered Backprojection Reconstruction

The attenuation coefficient is reconstructed using a filtered backprojection (FBP) formula developed in our previous work.³ Assuming that the reconstruction grid is infinitesimally fine (*i.e.*, non-pixelated), the FBP reconstruction is

$$\mu_{\text{FBP}}(\mathbf{r}) = \sum_{\mathbf{m}, n} F_{\mathbf{m}n}(\mathbf{r}), \quad (12)$$

where

$$F_{m^{\text{th}}}(\mathbf{r}) = \frac{\mathcal{D}\mu(\mathbf{m}, n)}{N} \cdot \left[\phi[t_1(\mathbf{r}, n)] * \text{rect}\left(\frac{t_1(\mathbf{r}, n) \cdot \sec[\theta(\mathbf{r}, n)] - m_x a_x}{a_x}\right) \right]_{t_1(\mathbf{r}, n) = x \cos[\theta(\mathbf{r}, n)] + z \cos[\Gamma(\mathbf{r}, n)] \sin[\theta(\mathbf{r}, n)]} \cdot \left[\text{rect}\left(\frac{t_2(\mathbf{r}, n) \cdot \sec[\theta(\mathbf{r}, n)] - (m_y + 1/2) \cdot a_y}{a_y}\right) \right]_{t_2(\mathbf{r}, n) = y \cos[\theta(\mathbf{r}, n)] + z \sin[\Gamma(\mathbf{r}, n)] \sin[\theta(\mathbf{r}, n)]} \quad (13)$$

Here, μ_{FBP} is the reconstructed attenuation coefficient, \mathbf{r} is a point in \mathbb{R}^3 , $\mathcal{D}\mu(\mathbf{m}, n)$ is signal in the \mathbf{m}^{th} detector element for the n^{th} projection, N is the total number of projections, ϕ is the filter, $*$ is the convolution operator, and (t_1, t_2) are affine parameters in the x-ray transform discussed in our previous work. In addition, the quantity $F_{m^{\text{th}}}(\mathbf{r})$ represents signal that is backprojected from the \mathbf{m}^{th} detector element to the point \mathbf{r} for the n^{th} projection. Our previous work also defined the concept of the azimuthal backprojection angle (Figure 2 in Acciavatti and Maidment³), which corresponds to the term $\Gamma(\mathbf{r}, n)$ in Eq. (13). According to the definition of $\Gamma(\mathbf{r}, n)$, it follows that

$$\cos[\Gamma(\mathbf{r}, n)] = \frac{u_1(n) - x_{\text{FS}}(n)}{\sqrt{[u_1(n) - x_{\text{FS}}(n)]^2 + [u_2(n) - y_{\text{FS}}(n)]^2}}, \quad (14)$$

$$\sin[\Gamma(\mathbf{r}, n)] = \frac{u_2(n) - y_{\text{FS}}(n)}{\sqrt{[u_1(n) - x_{\text{FS}}(n)]^2 + [u_2(n) - y_{\text{FS}}(n)]^2}}. \quad (15)$$

In order to evaluate Eqs. (14)-(15), one must solve for $u_1(n)$ and $u_2(n)$ using Eq. (5) as follows.

$$u_1(n) = \frac{x \cdot z_{\text{FS}}(n) - z \cdot x_{\text{FS}}(n)}{z_{\text{FS}}(n) - z} \quad (16)$$

$$u_2(n) = \frac{y \cdot z_{\text{FS}}(n) - z \cdot y_{\text{FS}}(n)}{z_{\text{FS}}(n) - z} \quad (17)$$

While our previous work calculated $\Gamma(\mathbf{r}, n)$ in a DBT system with focal spot motion restricted to the plane of the chest wall, Eqs. (14)-(17) provide a more general formulation for all possible focal spot positions.

3. RESULTS

3.1 Conventional Focal Spot Motion

In Figure 4, the reconstruction of a Defrise phantom is simulated for a conventional acquisition geometry, assuming that $N = 15$, $\varepsilon = 50.0$ mm, $C = 1/\varepsilon = 0.02$ mm⁻¹, $z_0 = 50.0$ mm, and $y_0 = 0$. The reconstruction is calculated at the mid-depth of the phantom ($z = z_0$), analogous to the experimental results. Also, the reconstruction technique is simple backprojection (SBP), for which there is no filtering. The focal spot positions for this geometry are

$$x_{\text{FS}}(n) = -\beta_1 v_n, \quad y_{\text{FS}}(n) = 0, \quad z_{\text{FS}}(n) = h, \quad v_n = \frac{2n}{N-1}, \quad n \in \left[-\frac{N-1}{2}, \frac{N-1}{2} \right], \quad (18)$$

where $\pm\beta_1$ is the projection range along the x direction, h is the source-to-image distance (SID), and v_n is a parameter that determines the focal spot position for the n^{th} projection. To ensure comparable tomographic properties as the DBT system that was used experimentally (Figures 1 and 2), the projection range along the x direction is the same as the Selenia Dimensions system; namely, $\beta_1 = h \cdot \sin(7.5^\circ) = 91.4$ mm. The geometry that is simulated has only a few small differences relative to the Selenia Dimensions system. In the Selenia Dimensions system, the x-ray tube traces a circular arc within the plane of the chest wall, and hence the SID varies with each projection. Conversely, in the geometry that is

simulated, the SID is constant ($h = 70.0$ cm). Also, while the Selenia Dimensions system has a rotating detector, the geometry that is simulated has a stationary detector.

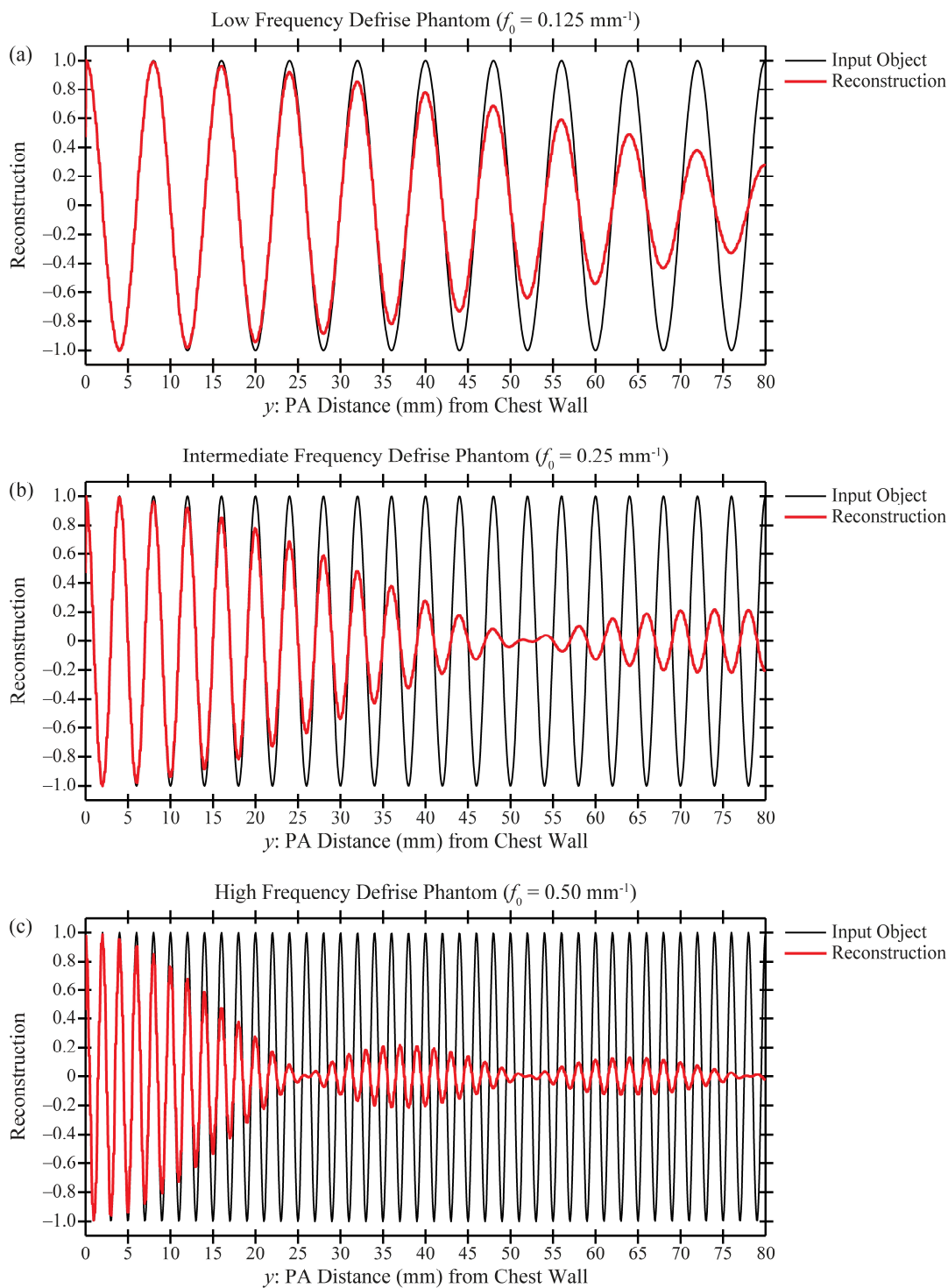


Figure 4. The reconstruction of a Defrise phantom is shown in a conventional DBT system. The amplitude of the reconstruction is degraded with increasing PA distance, indicating a loss of image quality.

Figure 4 shows that the peaks and troughs in the reconstruction decrease in amplitude with increasing PA distance. This result indicates that image quality is anisotropic along the PA direction, as expected from the experimental results (Figures 1 and 2). The anisotropy becomes more pronounced with increasing frequency. To quantify the image quality, modulation can be determined by normalizing the amplitude of the reconstruction against the corresponding signal of a zero frequency object. Figure 5 shows that, for a low frequency Defrise phantom ($f_0 = 0.125 \text{ mm}^{-1}$), modulation decreases with PA distance but is well above zero in the range of PA positions between 0 and 80.0 mm. By contrast, for intermediate and high frequency Defrise phantoms (0.25 and 0.50 mm^{-1} , respectively), modulation falls to zero at 52.0 and 26.0 mm, respectively. Because the analytical model simulates different input frequencies than the experimental results, the zeros of the modulation are not necessarily expected to match exactly the ones shown in Figure 2(b).

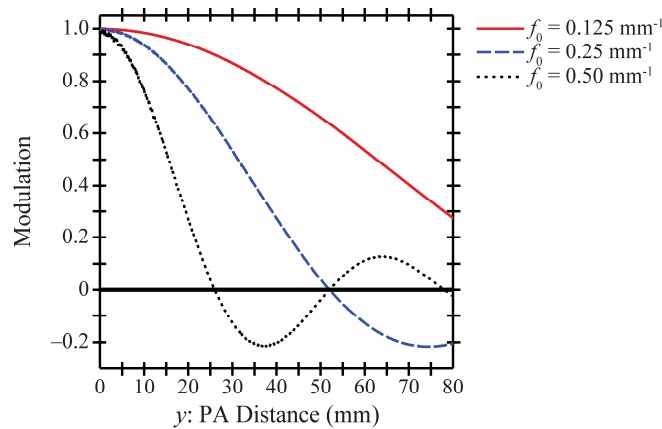


Figure 5. Modulation in the reconstruction of a Defrise phantom is degraded with increasing PA distance. This trend is more pronounced with increasing frequency.

In addition, the sign of the modulation can be analyzed as a separate measure of image quality in Figure 5. A change in sign indicates a 180° phase shift in the reconstructed waveform relative to the input waveform, demonstrating that the Defrise phantom is not properly represented in the image. Figure 5 shows that, while the low frequency Defrise phantom has no phase shift, the intermediate and high frequency Defrise phantoms have phase shifts. The phase shifts for these phantoms lie in the range $[52.0, 104.0] \text{ mm}$ and $[26.0, 52.0] \text{ mm}$, respectively. The full range of phase shifts is not shown in Figure 5 for the intermediate frequency phantom (dashed blue curve), since the plot is truncated at 80.0 mm. In summary, the image quality along the PA direction becomes poorer with increasing frequency.

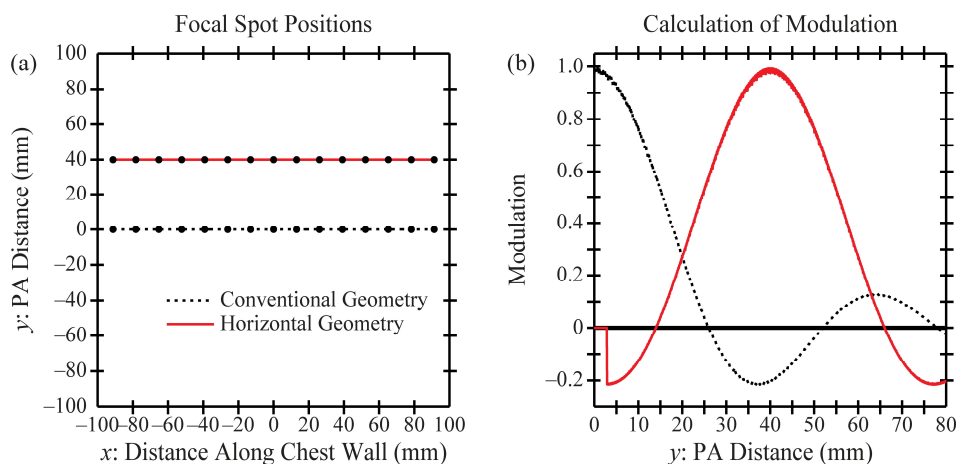


Figure 6. For the high frequency Defrise phantom ($f_0 = 0.50 \text{ mm}^{-1}$), the horizontal geometry yields improvements in modulation at positions distal to the chest wall. However, this geometry is ultimately rejected from consideration as a candidate, as it introduces a region of missed tissue coverage between 0 and 2.8 mm.

3.2 Constant Shift in Focal Spot Positions Along the PA Direction

To improve image quality along the PA direction, one might initially consider an acquisition geometry in which the focal spot positions are all displaced by a fixed increment along the PA direction. As such, the focal spot positions are similar to Eq. (18) but the y -coordinate must be modified so that $y_{FS}(n) = \beta_2$, where β_2 is the constant shift in the focal spot positions along the PA direction. In order to evaluate the image quality in this acquisition geometry, it is sufficient only to consider the high frequency Defrise phantom ($f_0 = 0.50 \text{ mm}^{-1}$), as this object exhibits the poorest image quality in the conventional acquisition geometry. Assuming that $\beta_2 = 40.0 \text{ mm}$, Figure 6(a) shows the focal spot positions in a plane parallel to the detector. In the figure, this geometry is termed the “horizontal” geometry, since the focal spot positions lie along a horizontal line in the plane shown. The 15 focal spot positions are denoted by points along this horizontal line. Figure 6(b) demonstrates that the horizontal geometry yields improvements in modulation at the positions distal to the chest wall. However, this geometry is characterized by loss of tissue coverage at the chest wall. In particular, the modulation is zero from 0 to 2.8 mm. This result can be deduced geometrically as shown in Figure 7, which provides a diagram of the missed tissue. Using similar triangles, one can prove that the region of missed tissue in Figure 7 perfectly matches the result determined in Figure 6(b); namely, $y_{CW} = \beta_2 z_0/h \approx 2.8 \text{ mm}$. In summary, although the horizontal geometry improves modulation at positions distal to the chest wall, this geometry is ultimately rejected from consideration as a candidate due to the loss of tissue coverage at the chest wall.

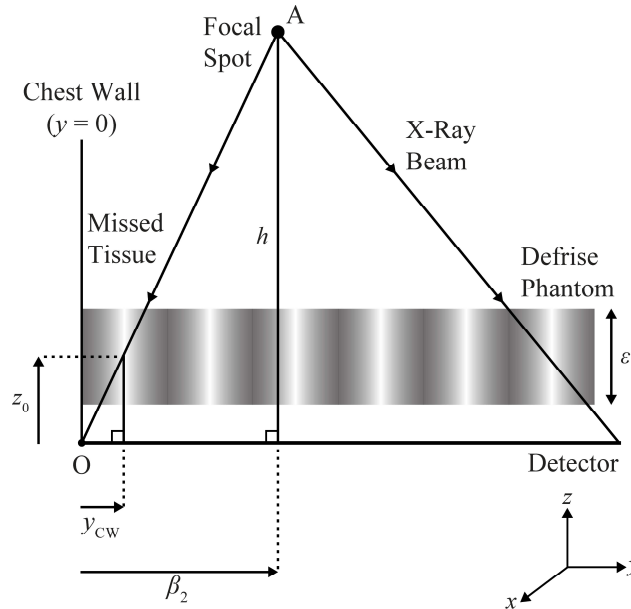


Figure 7. Introducing a translational shift in the position of the focal spot along the PA direction creates a region of missed tissue, which can be calculated from similar triangles.

3.3 Linear Focal Spot Motion Along the PA Direction

To improve tissue coverage at the chest wall, an acquisition geometry with linear focal spot motion along the PA direction is now considered [Figure 8(a)]. The focal spot positions are similar to Eq. (18), but the y -coordinate is modified so that $y_{FS}(n) = \beta_3 \cdot (1 - v_n)/2$, where β_3 is the maximum y -coordinate of the focal spot (*i.e.*, the apex coordinate). Because one projection is acquired in the plane of the chest wall (namely, $y = 0$), there is no loss of tissue coverage in the reconstruction, and hence the modulation is non-zero at positions that are proximal to the chest wall [Figure 8(b)]. Increasing the apex coordinate of the focal spot broadens the positions with positive modulation (*i.e.*, no phase shift). One drawback of this geometry is the sharp drop in modulation at positions proximal to the chest wall. For example, in the geometry with a 60.0 mm apex coordinate, modulation falls to 28% at 4.3 mm from the chest wall. This result arises due to missed tissue between 0 and 4.3 mm in some of the individual projections for which the focal spot is distal to the chest wall. In Section 3.4, a higher-order x-ray tube trajectory is modeled in order to minimize the drop in modulation at positions proximal to the chest wall.

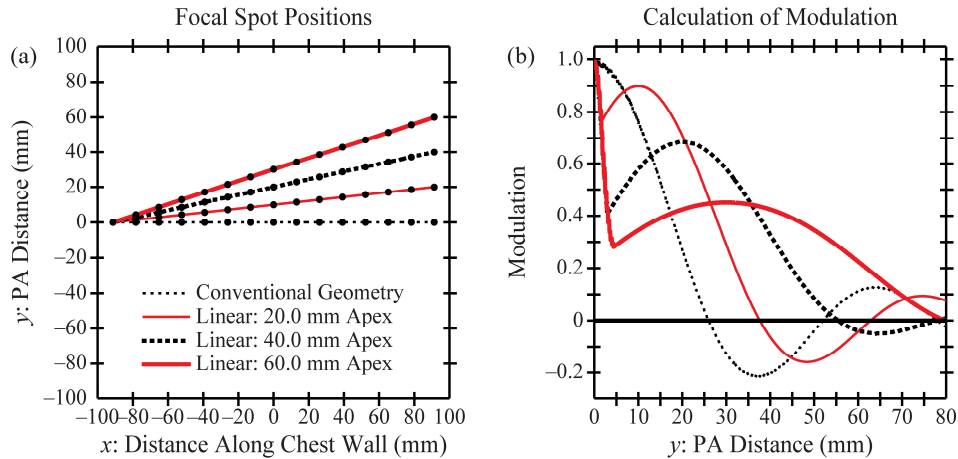


Figure 8. By introducing linear focal spot motion along the PA direction, the modulation of the high frequency Defrise phantom is improved at positions distal to the chest wall. However, the trade-off is a sharp drop in modulation at positions proximal to the chest wall.

3.4 Higher-Order Focal Spot Motion Along the PA Direction

Figure 9 shows a higher-order x-ray tube trajectory which follows the shape of the conchoid of de Sluze⁴ in a plane parallel to the detector. This trajectory has tails that are asymptotic to the chest wall, and has a loop anterior to the chest wall. Based on the position of the tails, this geometry is being investigated as a technique that minimizes the loss of modulation at the chest wall. The focal spot positions can be determined from the equations

$$x_{FS}(n) = q \left[(p_1 - p_3) \cos v_n - (p_2 - p_3) \sec v_n \right] \sin v_n \quad (19)$$

$$y_{FS}(n) = \left[(p_1 - p_3) \cos v_n - (p_2 - p_3) \sec v_n \right] \cos v_n + p_2 \quad (20)$$

$$z_{FS}(n) = h, \quad (21)$$

where $v_n \in [-\pi/2, \pi/2]$. Many of the parameters in Eqs. (19)-(20) are not commonly used in the formula for a conchoid, and are introduced here to offer greater control over the shape of the trajectory. More specifically, p_1 is the y -coordinate of the point most anterior to the chest wall (*i.e.*, apex), p_2 is the y -coordinate of the double point (*i.e.*, crunode), p_3 is the y -coordinate of the asymptote, and q is a dimensionless parameter controlling the area of the loop. Assuming that the first and last focal spot positions in the scan occur in the plane of the chest wall (*i.e.*, the plane for which $y = 0$), it can be shown that

$$p_3 = \frac{-p_1 p_2^2 q^2}{\beta_1^2}, \quad (22)$$

where $\pm\beta_1$ is the projection range along the x direction similar to all other geometries considered in this work.

Figure 9 shows the 15 focal spot positions along this trajectory. The 15 points are chosen so that eight focal spot positions lie along the tails, and seven focal spot positions lie along the loop. In each of the two tails, the four focal spot positions are equally spaced along the x direction. Similarly, the focal spot positions in the loop are equally spaced along the y direction. To determine the values of the parameter v_n corresponding to each of the 15 focal spot positions, MATLAB (Version R2012b, Natick, MA) was used to calculate the values numerically. Optimizing the choice of focal spot positions along the conchoid remains the subject of future work.

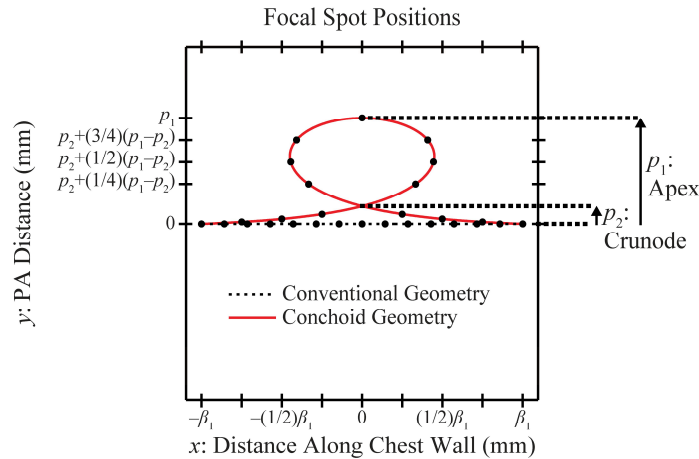


Figure 9. A diagram of the conchoid geometry is shown. Modulation at positions distal to the chest wall can be controlled by the apex coordinate (p_1). By contrast, modulation at positions proximal to the chest wall can be controlled by the crunode coordinate (p_2).

To study the effect of various parameters of the conchoid, a plot of modulation versus position is shown in Figure 10 for the high frequency Defrise phantom. The plot illustrates the effect of p_1 on modulation, assuming $p_2 = 5.0$ mm, $q = 2.0$, and $\beta_1 = 91.4$ mm. Three values of p_1 are considered (20.0, 40.0, and 60.0 mm). Recall that p_1 is the apex coordinate of the conchoid. Figure 10 shows that increasing the value of p_1 broadens the positions with positive modulation (*i.e.*, no phase shift), giving rise to an improvement in image quality. The loss of modulation at the chest wall is much less pronounced than the linear geometry (Section 3.3).

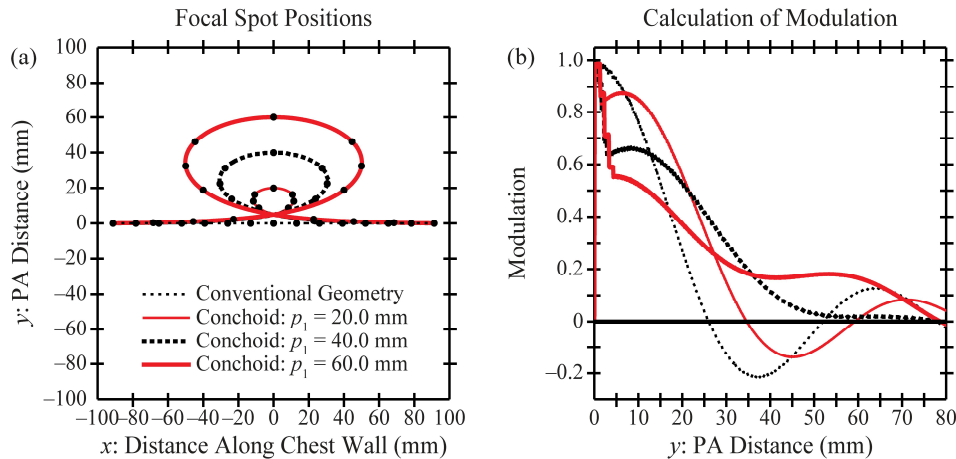


Figure 10. Increasing the value of p_1 gives rise to improvements in modulation at positions distal to the chest wall. However, the trade-off is reducing modulation at positions proximal to the chest wall.

It is also useful to consider the effect of increasing p_2 with constant p_1 (60.0 mm), as shown in Figure 11. Three values of p_2 are considered (5.0, 15.0, and 25.0 mm). Recall that p_2 is the y -coordinate of the crunode. Figure 11 indicates that increasing the value of p_2 yields increased modulation at positions distal to the chest wall, but presents the trade-off of reduced modulation at positions proximal to the chest wall. Thus, modulation can be optimized by varying the parameters of the x -ray tube trajectory.

To demonstrate one benefit of the conchoid geometry over the linear geometry, the loss of modulation at 4.3 mm from the chest wall can be calculated. While the modulation falls to 28% in the linear geometry with a 60.0 mm apex coordinate [Figure 8(b)], the modulation falls to 55%, 50%, and 43% in the conchoid geometries with the same apex coordinate ($p_2 = 5.0, 15.0,$ and 25.0 mm, respectively). In short, the loss of modulation at the chest wall is minimized by all three conchoid trajectories shown in Figure 11.

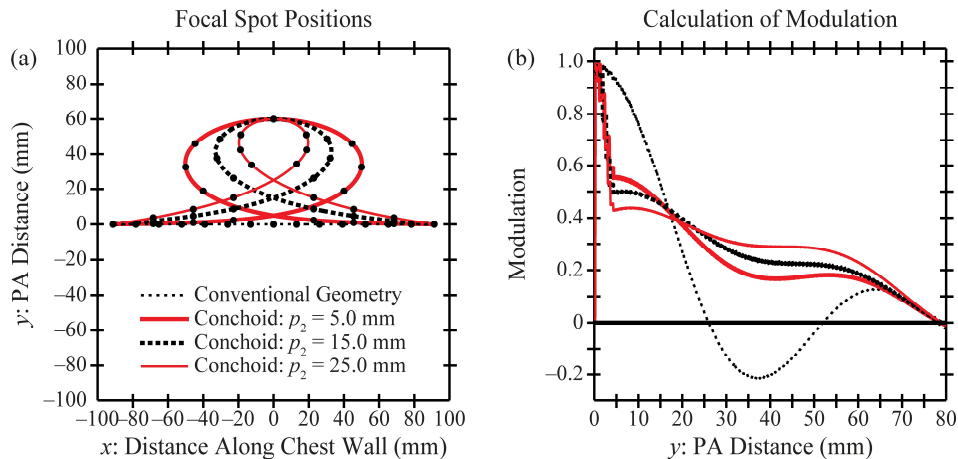


Figure 11. Similar to p_1 , increasing the value of p_2 yields an increase in modulation at positions distal to the chest wall, but a decrease in modulation at positions proximal to the chest wall.

4. DISCUSSION AND CONCLUSION

This work demonstrates that the Defrise phantom can be used to analyze the spatial anisotropy of image quality in DBT reconstructions. A physical phantom was constructed to demonstrate this property experimentally using the Selenia Dimensions system. It was shown that, while image quality is preserved at various positions along the tube travel direction (x), image quality is poorer with increasing position along the PA direction (y). In simulations, we demonstrate that image quality can be improved by introducing focal spot motion along the PA direction. Existing systems lack this component of motion. While multiple geometries were considered in the simulations, many of the candidate geometries were ultimately rejected from consideration as they have prohibitively low modulation at positions proximal to the chest wall. In particular, the horizontal geometry yields a region of missed tissue [Figures 6(b) and 7], and the linear geometry yields an abrupt drop in modulation at positions proximal to the chest wall [Figure 8(b)]. A conchoid geometry was investigated as an alternative technique that minimizes the loss of modulation at the chest wall based on the positioning of the tails of the x-ray tube trajectory (Figure 9). The conchoid geometry offers improvements in modulation at the distal PA positions, and minimizes the loss of modulation at the proximal PA positions.

Although a general reconstruction filter is included in the analytical model (Section 2.2), the simulations in Section 3 are performed with SBP reconstruction for which there is no filtering. In the linear systems (LS) model for DBT, Zhao showed that the zeros of the modulation are unaffected by the choice of filter; the filter only controls the relative modulation at each frequency.⁵ For this reason, in modeling a fixed input frequency ($f_0 = 0.50 \text{ mm}^{-1}$), as is the case in Sections 3.2-3.4, we would not expect the filter to improve the zeros of the modulation and hence to improve the anisotropies. Thus, it is acceptable to compare the benefits of the candidate geometries using SBP.

One limitation of the LS model is that it does not consider the effect of object thickness at each input frequency. In order to support the claim that the zero of the modulation is unaffected by the choice of filter, future work should calculate the modulation as a function of object thickness. In addition, future work should also study how the reconstruction filter should be optimized for the newly proposed geometries. In existing DBT systems with tube motion restricted to the plane of the chest wall, filtering is typically applied in only one direction (x). In a system with tube motion along the PA direction, future work should consider the potential merit of additional filtering along the PA direction (y).

In Sections 2 and 3, a DBT system with step-and-shoot motion is simulated. Future work should model continuous motion of the x-ray tube during the scan time. Because the conchoid geometry requires a greater total path length for the tube motion than the conventional geometry, an important trade-off is expected in a system with continuous tube motion. If the tube speed is maintained, the scan time must increase, yielding increased potential for patient motion. Conversely, if scan time is maintained, the x-ray tube must move more quickly, yielding increased focal spot blurring. Future work should calculate the loss of modulation due to tube motion in a conchoid geometry. In the event that this problem becomes significant, our previous work demonstrated that the velocity profile of the x-ray tube can be optimized.⁶ Unlike existing systems with a constant tube speed during the scan time, our previous work considered an oscillatory

tube speed that is large between projections and smoothly approaches zero during each projection. In simulations, our previous work has shown that the oscillatory source speed can be used to minimize focal spot blurring.

An analogy can be drawn between the Defrise phantom and dense fibroglandular tissue, since the extent of the phantom along the z direction is comparable to the breast thickness and the frequency is comparable to the spacing between dense tissue. Using computer breast phantoms with ground truth,⁷ future work should determine whether dense tissue is better quantified with a conchoid geometry. The computer phantoms should also be used to optimize the choice of focal spot positions. While this paper is limited to x-ray tube trajectories that are planar due to the constant SID, the computer breast phantom should be used to determine whether image quality is optimized by non-planar trajectories.

Additional directions for future modeling are now noted. Although the focal spot is treated as point-like in this paper, future work should model the loss of modulation with increasing focal spot size.⁸ Future work should also model oblique x-ray incidence.⁹⁻¹² At the distal PA positions on the detector, one would expect increasing deviation in the angle of x-ray incidence relative to the normal, and hence poorer modulation. Finally, while collimation is not simulated in Sections 2 and 3 of this paper, future work should determine how collimation can be optimized in new geometries.

5. ACKNOWLEDGEMENT

The authors are grateful to Baorui Ren (Hologic Inc., Bedford, MA) and others at Hologic for their discussions concerning technical information about the Selenia Dimensions system. In addition, we thank Predrag Bakic (University of Pennsylvania, Philadelphia, PA) and Yohei Matsutani (Japan Patent Office, Tokyo, Japan) for assistance with acquiring experimental images. Finally, we thank Johnny Kuo, Susan Ng, and Peter Ringer (Real Time Tomography, Villanova, PA) for sharing their technical expertise in image reconstruction. A.D.A.M. is a member of the scientific advisory board of Real Time Tomography. The project described was supported by a grant from the Bassler Research Center for BRCA in the Abramson Cancer Center at the University of Pennsylvania. The content is solely the responsibility of the authors and does not necessarily represent the official views of the funding agency.

6. REFERENCES

1. Mazin SR, Pelc NJ. Fourier rebinning algorithm for inverse geometry CT. *Medical Physics*. 2008;35(11):4857-4862.
2. Lee DL, Cheung LK, Rodricks B, Powell GF. Improved imaging performance of a 14 x 17-inch Direct Radiography (TM) System using Se/TFT detector. Paper presented at: SPIE Conference on Physics of Medical Imaging, 1998; San Diego, CA.
3. Acciavatti RJ, Maidment ADA. Observation of super-resolution in digital breast tomosynthesis. *Medical Physics*. 2012;39(12):7518-7539.
4. Dziok J, Raina RK, Sokol J. Certain results for a class of convex functions related to a shell-like curve connected with Fibonacci numbers. *Computers and Mathematics with Applications*. 2011;61:2605-2613.
5. Zhao B, Zhao W. Three-dimensional linear system analysis for breast tomosynthesis. *Medical Physics*. 2008;35(12):5219-5232.
6. Acciavatti RJ, Bakic PR, Maidment ADA. Proposing a New Velocity Profile for Continuous X-Ray Tube Motion in Digital Breast Tomosynthesis. Paper presented at: SPIE Medical Imaging, 2013; Lake Buena Vista, FL.
7. Pokrajac DD, Maidment ADA, Bakic PR. Optimized generation of high resolution breast anthropomorphic software phantoms. *Medical Physics*. 2012;39(4):2290-2302.
8. Johns HE, Cunningham JR. Chapter 16: Diagnostic Radiology. *The Physics of Radiology*. 4th ed. Springfield, IL: Charles C Thomas; 1983:557-669.
9. Acciavatti RJ, Maidment ADA. Calculation of OTF, NPS, and DQE for Oblique X-Ray Incidence on Turbid Granular Phosphors. *Lecture Notes in Computer Science*. 2010;6136:436-443.
10. Freed M, Park S, Badano A. A fast, angle-dependent, analytical model of CsI detector response for optimization of 3D x-ray breast imaging systems. *Medical Physics*. 2010;37(6):2593-2605.
11. Badano A, Freed M, Fang Y. Oblique incidence effects in direct x-ray detectors: A first-order approximation using a physics-based analytical model. *Medical Physics*. 2011;38(4):2095-2098.
12. Acciavatti RJ, Maidment ADA. Optimization of phosphor-based detector design for oblique x-ray incidence in digital breast tomosynthesis. *Medical Physics*. 2011;38(11):6188-6202.